Journal of Power Sources 278 (2015) 506–521

Contents lists available at ScienceDirect

Journal of Power Sources

journal homepage: www.elsevier.com/locate/jpowsour

Development of a physics-based degradation model for lithium ion polymer batteries considering side reactions

Rujian Fu [a], Song-Yul Choe [a, *], Victor Agubra [b], Jeffrey Fergus [b]

[a] 1418 Wiggins Hall, Mechanical Engineering, Auburn University, Auburn, AL, USA
[b] 273 Wilmore Laboratories, Materials Research and Education Center, Auburn University, Auburn, AL, USA

HIGHLIGHTS

- The degradations caused by side reactions are modeled using physical principles.
- Loss of ions and active anode materials are the factors that cause capacity fade.
- Simulated growths of SEI and deposit layers are validated by EIS and SEM analysis.
- Charging at high SOC accelerates the degradation processes.
- The effect of charging C-rates on overall degradation is not clearly distinctive.

ARTICLE INFO

Article history:
Received 27 October 2014
Received in revised form
8 December 2014
Accepted 15 December 2014
Available online 16 December 2014

Keywords:
Li ion polymer battery
Modeling of side reactions
Physics-based degradation model
Capacity fade
Loss of ion and active material
SEI

ABSTRACT

Experimental investigations conducted on a large format lithium ion polymer battery (LiPB) have revealed that side reactions taking place at anode are the major factor for degradation of the battery performance and lead to capacity and power fade. Side reactions consume ions and solvents from the electrolyte and produce deposits that increase the thickness of the solid electrolyte interphase (SEI) layer and form a new layer between composite anode and separator. These phenomena are described using physical principles based on the Tafel and Nernst equations that are integrated into the developed electrochemical-thermal model. The key parameters for the side reactions used in the model are experimentally determined from self-discharging behavior of the battery. The integrated model is then validated against experimental data obtained from different operating conditions. Analysis has revealed that the capacity fade is predominantly caused by loss of ions and active materials. The results also show that the rate of side reactions and degradations are more severe at charging process under high SOC and high C-rate due to low overpotential of the side reactions.

1. Introduction

The lithium ion battery has become one of the most widely used energy storage devices because of its high energy and power densities. The performances of lithium ion batteries can degrade over the required lifetimes, which can be defined by calendar or cycle life. The calendar life is affected by the self-discharging rate, while the cycle life is affected by operating conditions. Researchers have investigated causes for the degradations and identified side reactions as the major one [1–9]. The studies show that the side reactions are caused by reduction process of electrolyte components, particularly on composite anode when the electrochemical potential is out of the stability window of the electrolyte. The reduction process consumes lithium ions and the electrolyte solvents and produces deposits. Two major side reactions taking place on the anode side produce products as follows [7];

$$2Li^+ + 2e^- + EC \rightarrow CH2 == CH2 + Li_2CO_3\downarrow \quad (1)$$

$$2Li^+ + 2e^- + 2EC \rightarrow CH2 == CH2 + (CH_2OCO_2Li)_2\downarrow \quad (2)$$

The products of the side reactions can form a very thin reaction layer that adheres to the surface of the anode particles. This thin layer, called solid electrolyte interphase (SEI) [8], is deliberately created during the initial charging cycles by manufacturers to slow down the side reactions. However, when side reactions continue

* Corresponding author.
E-mail address: choe@auburn.edu (S.-Y. Choe).

http://dx.doi.org/10.1016/j.jpowsour.2014.12.059
0378-7753/

Nomenclature

A	sandwich area of the cell (cm^2)
a_s	specific surface area of electrode (cm^{-1})
c_s	ion concentration in solid phase (mol L^{-1})
c_e	ion concentration in electrolyte (mol L^{-1})
$C_{ionloss}$	Amount of ion loss caused by the side reactions (A h)
C_p	heat capacity (J kg^{-1} K^{-1})
D	diffusion coefficient (cm^2 s^{-1})
EOC	end of charge
EOD	end of discharge
E_{chem}	electrochemical energy (J cm^{-3})
F	Faraday constant (96,487C mol^{-1})
h_c	convective heat transfer coefficient (W cm^{-2} K^{-1})
I	current of the cell (A)
i	current density (A cm^{-2})
i_0	exchange current density of intercalation (A cm^{-2})
$i_{0,side}$	exchange current density of the side reactions (A cm^{-2})
j^{Li}_{total}	total reaction rate (A cm^{-2})
j^{Li}	reaction rate of intercalations (A cm^{-2})
j^{Li}_{side}	reaction rate of side reactions (A cm^{-2})
L	thickness of micro cell (cm)
l	coordinate along the thickness of micro cell
n	number of lithium ions
OCV	open circuit voltage (V)
P_{chem}	power contributing to the increase of chemical energy (W cm^{-3})
Q	capacity of the cell (A h)
Q_{aged}	capacity of an aged cell (A h)
Q_{fade}	capacity fade (A h)
$Q_{fade,ion}$	capacity fade due to loss of ion (A h)
$Q_{fade,AM}$	capacity fade due to loss of active anode material (A h)
q_{rev}	reversible heat generation rate (W cm^{-3})
q_{irr}	irreversible heat generation rate (W cm^{-3})
q_{convec}	heat convection rate (W cm^{-3})
R	resistance (Ω cm^2) or universal gas constant (8.3143 J mol^{-1} K^{-1})
r_s	radius of spherical electrode particle (cm)
r	coordinate along the radius of electrode particle (cm)
SOC	state of charge
T	cell temperature (K)
T_∞	ambient temperature (K)
U_{equi}	equilibrium potential (V)
V	voltage (V) or volume of the composite electrode (cm^3)
x	stoichiometric number in anode
y	stoichiometric number in cathode
t^0_+	initial transference number

Greek symbols

α	transfer coefficient for an electrode reaction
δ	thickness (cm)
ε	volume fraction of a porous medium
ϕe	potential in electrolyte phase (V)
ϕs	potential in solid phase (V)
η	surface overpotential of electrode reaction (V)
κ	ionic conductivity of electrolyte (S cm^{-1})
κ_D	concentration driven diffusion conductivity (A cm^{-1})
σ	conductivity (S cm^{-1})

Subscripts

AM	active (anode) material
a	anodic
c	cathodic
cc	current collector
$cell$	micro cell
DL	deposit layer
EIS	measured by EIS
e	electrolyte phase
max	maximum
$-$	negative electrode (anode)
$+$	positive electrode (cathode)
r	radial direction in electrode particle
SEI	solid-electrolyte interphase
SEM	measured by SEM
s	solid phase
$side$	side reactions
T	terminal
0%	0% state of charge
100%	100% state of charge

Superscripts

eff	effective
Li	Lithium ion

during cycling over a long time scale, the produced deposits are accumulated in the SEI and consequently lead to growth of the SEI [1,4,10,11].

The deposits are ionic conductors, but the ionic conductivity is relatively small. Therefore growth of the SEI leads to increase in ionic resistance and power fade. By contrast, these deposits are electronic isolators [7,8,10] that can electrically isolate some carbon particles, so that these isolated particles cannot participate in the electrochemical reactions, which causes loss of active carbon material and leads to capacity fade [3,4,7,12,13]. In addition, the ions consumed by the side reactions cannot participate in the electrochemical reactions, which contributes to capacity fade [1,14].

Our previous work that experimentally investigated the degradation processes of NMC/Carbon LiPB [9] using SEM, XRD and XPS verified that the predominant degradation is caused by the deposits from the side reactions at anode. This finding is based on the increase in the SEI resistances measured by electrochemical impedance analysis (EIS) correlating with the formation of new deposit layers between the composite anode and separator measured by scanning electron microscopy (SEM). No significant changes in active materials on both electrodes were observed at cycled cells [9]. The importance of side reactions indicated by our previous work is consistent with experimental findings published in literature [1,3,4,7,8,10–14].

Analysis of effects of side reactions on degradation of a battery has been performed using electrochemical-thermal model by changing internal parameters subject to degradation processes. Some authors extracted the values for the parameters by fitting performance of the model to the experimental data obtained at different number of cycles [3,5,6,9,12]. However, the results of these semi-empirical models deviate from experimental data when operating conditions are changed, which limits use of the model to real applications.

Therefore, there has been several attempts to develop physics-based degradation models based on electrochemical principles for the side reactions [1,2,4,13,14]. Doyle et al. were the first

research group to describe the side reactions using the Tafel equation, but no simulation was carried out [2]. Ramadass et al. extended Doyle's model and simulated capacity fade caused by loss of ions [1]. Sikha proposed a similar model for the side reactions, where the effect of deposits on the porosity is considered [4]. Ning et al. then validated Sikha's model using experimental data, which is obtained by cycling the cell under small current (1C) only [14]. Safari et al. has extended the model to consider the diffusion of the electrolyte solvent in the SEI [13], but they did not provide experimental data that proves the effects of such diffusion process on degradation. Although the previous aforementioned work attempted to physically describe the side reactions and formation of the SEI, the formation of deposit layers or loss of electrolyte solvents identified as two important degradation processes in the experimental work [9,15] are not considered in their modeling efforts. In addition, the exchange current density and equilibrium potential of the side reactions used assumed values [1,2,4,13,14].

The degradation process caused by the side reactions depends upon operating conditions, such as state of charge (SOC), C-rate and temperature [3,9], which have not been well analyzed. Doyle showed a dependence of degradation on SOC [1], but did not consider the effects of C-rates nor provide any experimental validations. In fact, self-discharging caused by side reactions [16–18] has not been analyzed using models.

Moreover, effects of side reactions on capacity fade have not yet been clarified. Since the side reactions are irreversible processes and consume lithium ions, some authors have claimed that capacity fade is caused by loss of ion and the amount of capacity fade is assumed to be the same as the amount of ion loss [1,14]. Others have attributed the capacity fade primarily to the loss of active carbon material due to SEI isolations [4,7,9] because the product of side reactions forms and electronically insulting SEI layer. More authors believed that loss of ion and loss of active material are both the two factors that lead to capacity fade [3,6,12,13,19], which were analyzed using semi-empirical models rather than physics-based principles.

In this work, a physics-based model for the side reactions has been developed considering formation of deposit layers and loss of electrolyte, and integrated into an electrochemical-thermal model developed previously. The integrated model is validated against experimental data obtained from a large format LiPB. Particularly, the exchange current density and equilibrium potential of the side reactions needed for the model are extracted from the self-discharging characteristics of the battery. Based on estimated loss of ion and loss of active material using the model, capacity fade is analyzed using equilibrium potentials. Finally, the integrated model is validated against experimental data obtained under cycling with different operating conditions that include SOC cycling limits and charging C-rates.

2. Model development

2.1. Electrochemical-thermal model without considering side reactions

The commercial LiPB cells studied in this work has a pouch type with dimensions of 164 mm × 250 mm × 5 mm. The single pouch cell has 15.7 A h capacity and is composed of 30 cells connected in parallel. The active material of the anode and cathode are carbon and NMC ($Li[MnNiCo]O_2$), respectively. The polymer separator is made of PVdF. The electrolyte salt is $LiPF_6$ and its solvents are ethylmethyl carbonates (EC) and dimethyl carbonate (DMC). Both electrode particles and the separator are mixed with the electrolyte.

The fresh cell is mathematically described by a one dimensional sandwiched model, which was developed in previous work [20,21]. The model is composed of a porous composite anode mixed with electrolyte, a separator and a porous composite cathode mixed with electrolyte. A schematic diagram is shown in the left of Fig. 1. When the cell is charged or discharged, electrons go through external circuit while ions are transported in the electrode and electrolyte. Chemical reactions take place at the surfaces of the electrode particles that contact the electrolyte and then ions diffuse into the electrode particles. The model has three temperature-dependent parameters including SEI resistance, diffusion coefficient of ions in the electrode particle and exchange current density of side reactions, whose temperature dependencies are obtained empirically based on experimental data. In addition, three heat source terms, change of entropy, Joule heating and heat of mixing, are considered. The equations summarized in Table 1.

2.2. Modeling of intercalation and side reactions

When side reactions take place at the interface between the electrode particles and the electrolyte, the reaction rates need to be modified by considering an extra rate induced by the side reactions. Intercalation reactions occur on both electrodes, while the side reactions occur only on the anode side. The total reaction rate, j^{Li}_{total}, is expressed as a sum of both reaction rates;

$$j^{Li}_{total} = j^{Li} + j^{Li}_{side} \tag{3}$$

where j^{Li} and j^{Li}_{side} denote the reaction rates caused by intercalation and side reactions, respectively.

The intercalation process can be modeled using the Butler–Volmer equation;

$$j^{Li} = i_0\left(\exp\left(\frac{\alpha_a nF}{RT}\eta\right) - \exp\left(-\frac{\alpha_c nF}{RT}\eta\right)\right) \tag{4}$$

where α_a and α_c are the symmetric factors of anodic and cathodic intercalation reactions, which take values of 0.5. n denotes the number of ions transferred in intercalation reaction which is equal to 1 for lithium ion.

To reduce computational time, Eq. (4) can be simplified to a linear form;

$$j^{Li} = i_0\frac{n(\alpha_a + \alpha_c)F}{R\cdot T}\eta \tag{5}$$

The activation overpotential of intercalation is

$$\eta = \phi_s - \phi_e - U_{eq} - R_{SEI}j^{Li}_{total} \tag{6}$$

where ϕ_s and ϕ_e are electrical potentials of the solid electrode particle and electrolyte, respectively. R_{SEI} is the resistance of SEI that

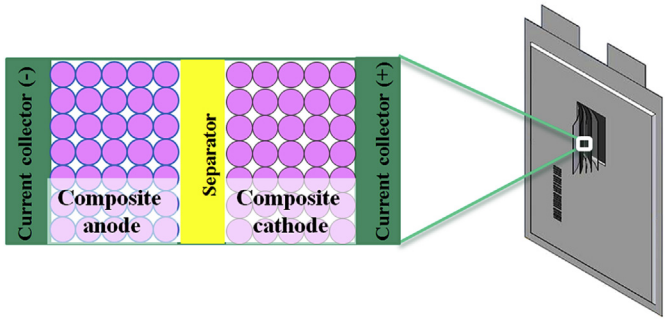

Fig. 1. Schematic diagram of the single cell (right) and micro cell (left) (the electrolyte is mixed with the composite electrodes and separator).

Table 1
Ion transport, charge conservation and energy equations.

Conservation equations	Boundary conditions
Ion conservation in electrode $\frac{\partial c_s}{\partial t} = D_s\left(\frac{\partial^2 c_s}{\partial r^2} + \frac{2}{r}\frac{\partial c_s}{\partial r}\right)$	$r^2\frac{\partial c_s}{\partial r}\Big\|_{r=0} = 0 \quad -D_s\frac{\partial c_s}{\partial r}\Big\|_{r=r_s} = \frac{j^{Li}}{F}$
Ion conservation in electrolyte $\frac{\partial(\varepsilon_e c_e)}{\partial t} = \frac{\partial}{\partial l}\left(D_e^{eff}\cdot\frac{\partial}{\partial l}c_e\right) + \frac{1-t_p^0}{F}a_s j^{Li} = 0$	$\frac{\partial c_e}{\partial l}\Big\|_{l=0} = \frac{\partial c_e}{\partial l}\Big\|_{l=L} = 0$
Charge conservation in electrode $\frac{\partial}{\partial l}\left(\sigma_s^{eff}\cdot\frac{\partial}{\partial l}\phi_s\right) = a_s j^{Li}$	$-\sigma_{s,n}^{eff}\frac{\partial\phi_s}{\partial l}\Big\|_{l=0} = -\sigma_{s,p}^{eff}\frac{\partial\phi_s}{\partial l}\Big\|_{l=L} = \frac{I}{A}\frac{\partial\phi_s}{\partial l}\Big\|_{l=\delta_n} = \frac{\partial\phi_s}{\partial l}\Big\|_{l=\delta_p} = 0$
Charge conservation in electrolyte $\frac{\partial}{\partial l}\left(\kappa_e^{eff}\cdot\frac{\partial}{\partial l}\phi_e\right) + \frac{\partial}{\partial l}\left(\kappa_D^{eff}\cdot\frac{\partial}{\partial l}\left(\ln c_e\right)\right) + a_s j^{Li} = 0$	$\frac{\partial\phi_e}{\partial l}\Big\|_{l=0} = \frac{\partial\phi_e}{\partial l}\Big\|_{l=L} = 0$
Energy equation	
Heat transfer (lumped model) $C_p m\frac{\partial T}{\partial t} = q_{rev} + q_{irr} + q_{convec}$ Irreversible heat generation rate $E_{chem} = -\varepsilon_{s+}\cdot F\cdot\int_V c_{s,p}\cdot U_{equi,p}\cdot dV - \varepsilon_{s,n}\cdot F\cdot\int_V c_{s,n}\cdot U_{equi,n}\cdot dV$ $p_{chem} = \frac{dE_{chem}}{dt}\quad q_{irr} = -V_T\cdot I - P_{chem}$ Heat convection $q_{convec.} = h_c(T - T_\infty)$	Reversible heat generation rate $q_{rev} = \int_V j^{Li}\cdot a_s\cdot T\cdot\frac{\partial U_{OCV}}{\partial T}dV$

is present only on the anode side. U_{eq} is the equilibrium potential of intercalation. In fact, U_{eq} is not just a function of stoichiometric number of the electrode, but also affected by ion concentration in electrolyte, according to the Nernst Equation;

$$U_{eq-} = U_{eq-}^{\Theta}\left(x\right) + \frac{RT}{nF}\ln\left(\frac{c_{e-}}{c_{e0}}\right) \tag{7}$$

$$U_{eq+} = U_{eq+}^{\Theta}\left(y\right) + \frac{RT}{nF}\ln\left(\frac{c_{e+}}{c_{e0}}\right) \tag{8}$$

where $U_{eq}^{\Theta}(x)$ and $U_{eq}^{\Theta}(y)$ are the standard equilibrium potentials when c_e is equal to c_{e0}.

The electrochemical-thermal model developed previously used an empirical polynomial that approximated $U_{eq}^{\Theta}(x)$ [20,21]. Since the approximation for $U_{eq}^{\Theta}(x)$ has some errors that result in inaccurate calculation of overpotential and side reaction rate, the polynomial has been replaced by a set of data provided by the manufacturer, which is plotted as the blue curve in Fig. 2 (in the web version). On the other hand, open circuit voltage (OCV) is measured experimentally, as plotted as green curve in Fig. 2. $U_{eq+}^{\Theta}(y)$ can be obtained from the relationship for OCV that is equal to the difference between the two equilibrium potentials on the cathode and anode;

$$OCV = U_{eq+}^{\Theta}\left(y\right) - U_{eq-}^{\Theta}\left(x\right) \tag{9}$$

The side reactions are irreversible since the rate of the reduction process is much larger than the oxidation process. Therefore, the side reactions are described using the Tafel equation;

$$j_{side}^{Li} = -i_{0,side}\exp\left(-\frac{\alpha_{c,side}n_{side}F}{RT}\eta_{side}\right) \tag{10}$$

where Tafel kinetics of the side reactions is assumed to be thermodynamically inconsistent because the reaction rate j_{side}^{Li} does not vanish as the overpotential η_{side} becomes zero. $i_{0,side}$ is the exchange current density of the side reactions, whose temperature dependency will be discussed later. n_{side} is the number of ions involved in the side reactions which is equal to 2, as seen in Eq. (1) and Eq. (2). The activation overpotential of the side reactions, η_{side}, are calculated as;

$$\eta_{side} = \phi_s - \phi_e - U_{eq,side} - R_{SEI}j_{total}^{Li} \tag{11}$$

where $U_{eq,side}$ is the equilibrium potential of the side reactions;

$$U_{eq,side} = U_{eq,side}^{\Theta} + \frac{RT}{n_{side}F}\ln\left(\frac{c_e}{c_{e0}}\right) \tag{12}$$

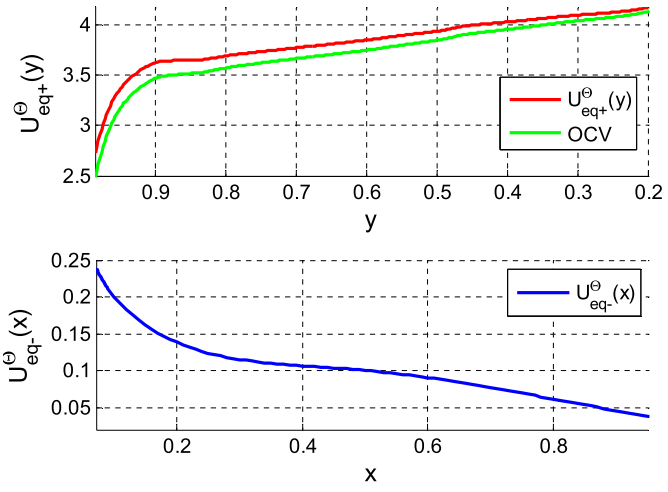

Fig. 2. Equilibrium potentials and OCV.

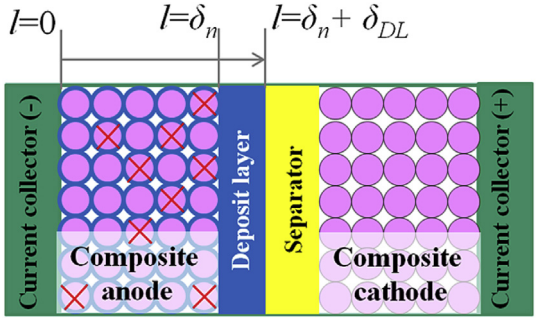

Fig. 3. Schematic diagram of a degraded cell.

Unlike $U^{\Theta}_{eq,\mathrm{int}}$, $U^{\Theta}_{eq,side}$ is independent on stoichiometric numbers and assumed to be a constant [1,4,13,14].

2.3. Effect of side reactions on degradation processes

Five degradation processes caused by the side reactions are modeled in this work and they are i) loss of ion, ii) growth of SEI, iii) loss of active anode material, iv) growth of deposit layer (DL) and v) loss of electrolyte. Three of them are graphically depicted in Fig. 3 (in the web version), where the thick blue circles, the particles marked with red "X" and the layer with blue color indicate SEI, loss of active material and formation of deposit layers, respectively.

The amount of ion loss, $C_{ionloss}$, can be obtained by integrating the side reaction rate, j^{Li}_{side}, over the volume of composite anode and time;

$$C_{ionloss}\left(\tau\right) = \int_{x=0}^{\delta_n}\left(\int_{t=0}^{\tau}\left|j^{Li}_{side}\left(l,t\right)\right|a_s dt\right)Adl \tag{13}$$

where $C_{ionloss}$ has a unit of A h, δ_n is the thickness of composite anode, τ is the total operating time and A is the cross section of the cell. a_s is the specific area of electrode with a unit of cm^{-1}, which indicates the area of active electrode in a unit volume of composite electrode.

The volume fraction of SEI, ε_{SEI}, is the volume of SEI in a unit volume of composite anode and expressed using the rate of side reactions;

$$\Delta\varepsilon_{SEI}\left(\tau,l\right) = \frac{\tilde{V}_{SEI}}{2F}\int_{t=0}^{\tau} j^{Li}_{side}\left(l,t\right)a_s dt \tag{14}$$

where $\tilde{V}_{SEI}$ is the molar volume of SEI. The coefficient 2 in the denominator indicates that consumption of 2 mol of ions produces 1 mol of SEI, according to Eqs. (1) and (2).

Since the rate of side reactions, j^{Li}_{side}, is a function of thickness l, ε_{SEI} also becomes a function of l. Given a ε_{SEI}, the thickness and resistance of SEI can be calculated as follows;

$$\Delta\delta_{SEI}\left(\tau,l\right) = \frac{\Delta\varepsilon_{SEI}(\tau,l)}{a_s} \tag{15}$$

$$\Delta R_{SEI}\left(\tau,l\right) = \frac{\Delta\delta_{SEI}(\tau,l)}{\kappa_{SEI}} \tag{16}$$

where κ_{SEI} is the ionic conductivity of SEI.

Loss of active materials is simply described using an empirical equation as follows;

$$\Delta\varepsilon_{s-}(\tau,l) = -k_{iso}{}^{*}\Delta\varepsilon_{SEI}(\tau,l) \tag{17}$$

where ε_s is the volume fraction of solid active material that is also dependent on thickness l. k_{iso} is a dimensionless coefficient which describes how fast the active anode materials are isolated from chemical reactions.

Since particles are glued together by binders that are mechanically resistive against the growth of SEI, SEI is very thin. In contrast, the DL is formed between the composite anode and the separator so it is much thicker in comparison with SEI [9]. The region that is responsible for the formation of DL can be regarded as the region of composite anode without binder, which is $\delta_n - R_s < l < \delta_n$, where R_s denotes the radius of anode particles that are adjacent to the separator. Thus, the increase in the thickness of DL is expressed with;

$$\delta_{DL}\left(\tau\right) = \frac{\tilde{V}_{DL}R_s}{2F}\int_{t=0}^{\tau} j^{Li}_{side}\left(\delta_n,t\right)a_s dt \tag{18}$$

When ionic current flows through the DL, extra voltage drop is induced due to its resistance that can be simply expressed by dividing its thickness by its ionic conductivity, κ_{DL};

$$R_{DL}\left(\tau\right) = \frac{\delta_{DL}(\tau)}{\kappa_{DL}} \tag{19}$$

As a result, the terminal voltage becomes as follows;

$$V_T = \phi_s|_{l=L} - \phi_s|_{l=0} - R_{cc}i - R_{DL}\int_0^{\delta_n} j^{Li}\left(l\right)a_s dl \tag{20}$$

where $\int_0^{\delta_n} j^{Li}(l)\,a_s dl$ denotes the ionic current passing through the DL. Eq. (20) has also considered the voltage drop on R_{SEI} because R_{SEI} affects the value of ϕ_s.

Loss of electrolyte solvent caused by side reactions is described using the volume fraction of electrolyte;

$$\Delta\varepsilon_{e-}\left(\tau\right) = -\frac{\alpha\tilde{V}_e C_{ionloss}\left(\tau\right)}{A\delta_n F} \tag{21}$$

where α is a coefficient indicating how many moles of electrolyte is consumed when 1 mol of lithium ion is consumed, which is equal to 0.5 for the side reaction in Eq. (1) and 1 for the side reaction in Eq. (2). Under the assumption that both side reactions have the same reaction rate, an averaged value of 0.75 is taken.

Since the effective diffusion coefficient of electrolyte is dependent on ε_e;

$$D^{eff}_e = D_e\cdot\varepsilon_e \tag{22}$$

Loss of electrolyte leads to a decrease in the diffusion rate in electrolyte.

The amount of charge participating in the degradation processes caused by the side reactions are the integration of j^{Li}_{side} over a given time and the measure for capacity and power fade, as seen in (13)–(22). However, the reaction rates can have different magnitudes at any instant, which is analyzed later in the section 5.

3. Determination of parameters for side reactions by analysis of self-discharge characteristics

As described in the previous section, the rate of the side reactions, j^{Li}_{side}, determines the rates of all corresponding degradation processes. According to Eq. (10), $i_{0,side}$ and $U_{eq,side}$ are the key parameters that affect j^{Li}_{side} and η_{side}, respectively. In addition, η_{side} determines j^{Li}_{side}, based on Eqs. (10) and (11). Both $i_{0,side}$ and $U_{eq,side}$ can be extracted from the self-discharging experimental data.

When a cell is resting under open circuit, the side reactions consume electrons based on the Eqs. (1) and (2). Since the electrolyte and separators are nonconductive for electrons, the electrons consumed by the side reactions are coming from anode particles (Li_xC_6). When one electron in Li_xC_6 is lost, Li_xC_6 should lose one lithium ion as well according to the law of charge conservation:

$$\mathrm{n}\cdot\mathrm{Li_xC_6} \rightarrow \mathrm{n}\cdot\mathrm{Li_{x-2/n}C_6} + 2\mathrm{Li^{+}} + 2\mathrm{e^{-}} \tag{23}$$

The consumed lithium ions are those de-intercalate from

anodes, which implies that a small amount of the current is induced by the main reaction between lithium ion and electrons of electrodes even under open circuit. Since the composite anode has no net current under open circuit, the total reaction rate, j^{Li}_{total}, is equal to zero. Then Eq. (3) yields

$$j^{Li}_{-} = -j^{Li}_{side} \tag{24}$$

$$j^{Li}_{+} = 0 \tag{25}$$

Eq. (24) shows that the rate of ion de-intercalating from anode particles is equal to the rate of ion being consumed by the side reactions. Therefore, the equilibrium potential of the anode increases due to reduced amount of ion in anode. On the other hand, since j^{Li}_{+} is equal to zero, the equilibrium potential of cathode remains the same. Hence, the OCV decrease under resting.

The mechanism described above is one of the major causes for self-discharge [16–18]. Although some work has reported other causes for self-discharge, such as separator leakage and dissolution of Mn from cathode [2], the investigated cells in this work have not shown evidence of these phenomena, so the side reactions are regarded as the only cause for self-discharge.

Since self-discharge is a slow process and its rate is only determined by the side reactions rather than major intercalation, the self-discharge characteristics are used to determine two key parameters, exchange current density, $i_{0,side}$, and equilibrium potential, $U_{eq,side}$, of the side reactions. The exchange current density of the side reactions is dependent upon temperature and experimentally determined by measurement of the self-discharge rate at different temperatures, i.e. 0 °C, 25 °C and 50 °C. Conversely, the equilibrium potential is not considered as temperature dependent within range of the experiments and determined by taking an average value of measured data at different temperatures.

The two values of the parameters are used to calculate the voltage change during self-discharge using the cell model, which is plotted with lines and compared with experimental data plotted with symbols in Fig. 4. The experimental data was collected in every several days for about two months. However, the computational time has taken too long to calculate the performance during the period, therefore only the self-discharge process for the first 50 days is calculated and shown in Fig. 4.

The values of $i_{0,side}$ and $U_{eq,side}$ obtained by fitting the self-discharge process are summarized in Table 2.

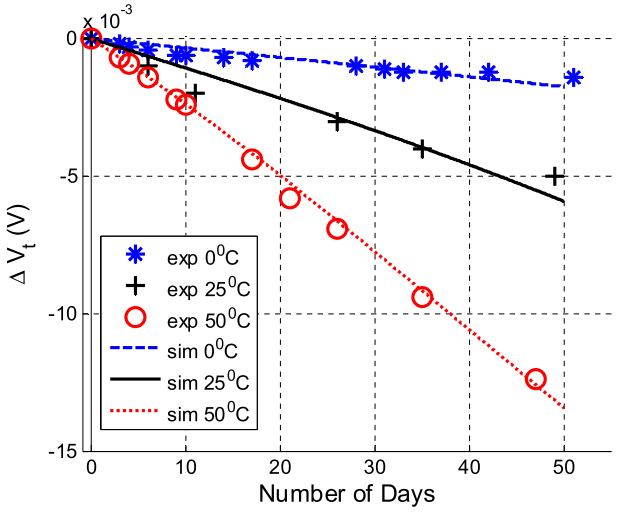

Fig. 4. Decrease in terminal voltages under self-discharge tests.

Table 2
Values of $i_{0,side}$ and $U_{eq,side}$ obtained from self-discharge characteristics.

	0 °C	25 °C	50 °C
$i_{0,side}$ (A cm^{-2})	0.39×10^{-11}	2.28×10^{-11}	6.50×10^{-11}
$U_{eq,side}$ (V)	0.21		

In this work, self-discharge caused by side reactions is considered an irreversible process, even though part of self-discharge can be reversible [17,18]. Since the major focus of this work is to study degradation processes caused by the irreversible side reactions, the mechanism of reversible self-discharge has not been considered and consequently its rate is assumed to be zero. This assumption results in a higher $i_{0,side}$ than the actual value.

4. Effect of side reactions on capacity fade

The consequences of the side reactions discussed in previous section are loss of ions, loss of active material, growth of SEI/DL, and loss of electrolyte. The first two factors cause capacity fade, while the last three factors lead to power fade. The power fade can be relatively simply predicted based on increased resistances. Therefore, only the relationship between capacity fade and the first two phenomena is analyzed with the help of equilibrium potentials. Equilibrium potentials for anode and cathode are functions of ion concentrations and can be expressed with stoichiometric numbers.

End-of-charge (EOC) and end-of-discharge (EOD) are defined as the points of the OCV that are equal to OCV_{max} and OCV_{min}, as provided by manufacturers, respectively. Capacity of a battery can be expressed with an amount of charges transferred from EOC to EOD and vice versa as follows;

$$\begin{aligned} Q &= (y_{EOD} - y_{EOC})\varepsilon_{s+}\delta_{+}Ac_{s,\max,+}F \\ &= (x_{EOC} - x_{EOD})\varepsilon_{s-}\delta_{-}Ac_{s,\max,-}F \end{aligned} \tag{26}$$

For a fresh cell, x_{EOC}, y_{EOC}, x_{EOD} and y_{EOD} correspond to x_{max}, y_{min}, x_{min} and y_{max}, respectively, so the capacity of a fresh cell is

$$\begin{aligned} Q_{fresh} &= (y_{\max} - y_{\min})\varepsilon_{s+}\delta_{+}Ac_{s,\max,+}F \\ &= (x_{\max} - x_{\min})\varepsilon_{s-}\delta_{-}Ac_{s,\max,-}F \end{aligned} \tag{27}$$

A relationship between x and y for a fresh cell can be then derived;

$$y = -\frac{\varepsilon_{s-}\delta_{-}c_{s,\max-}}{\varepsilon_{s+}\delta_{+}c_{s,\max+}}(x - x_{\min}) + y_{\max} \tag{28}$$

The values of x_{max}, y_{min}, x_{min} and y_{max} are provided by the manufacturer. The equilibrium potentials of a fresh cell are plotted versus stoichiometric number in Fig. 5 (in the web version), where EOC and EOD are marked with black "X". The OCV is plotted as green curve in Fig. 5.

4.1. Effect of loss of ions on capacity fade

When ions are lost because of side reactions at anode, the actual stoichiometric number on the anode side, x, is less than that of the fresh cell. The resulting x is a sum of the previous x with x_{shift}, as expressed below;

$$y = -\frac{\varepsilon_{s-}\delta_{-}c_{s,\max-}}{\varepsilon_{s+}\delta_{+}c_{s,\max+}}\left(x + x_{shift} - x_{\min}\right) + y_{\max} \tag{29}$$

where x_{shift} is the amount of shift in x axis, which is graphically depicted in Fig. 6. x_{shift} is expressed with the amount of ion loss;

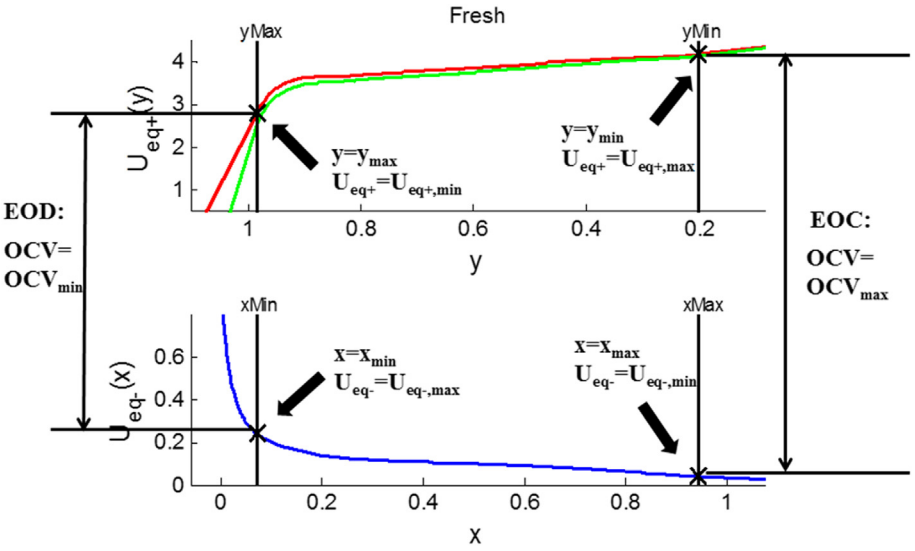

Fig. 5. Equilibrium potentials with EOC and EOD of a fresh cell.

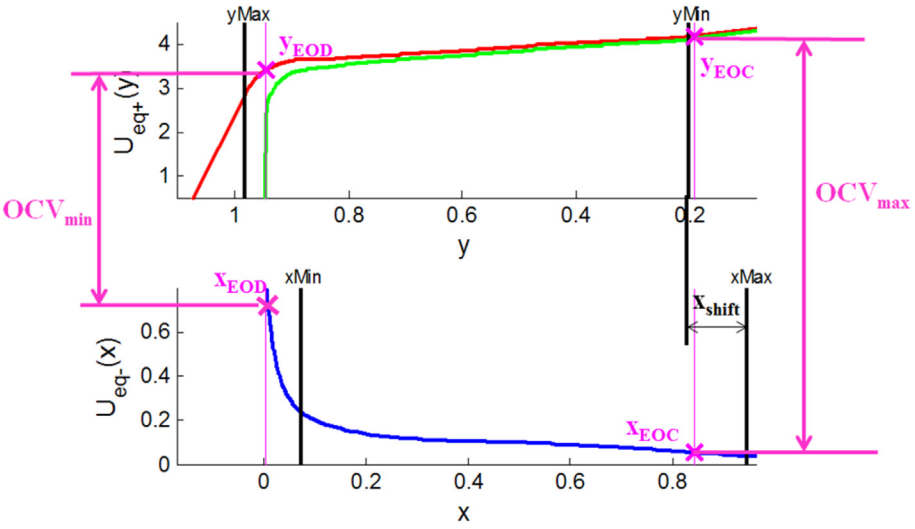

Fig. 6. Equilibrium potentials with EOD and EOC for an aged cell after loss of ion.

$$x_{shift} = \frac{C_{ionloss}}{\varepsilon_{s-}\delta_{-}Ac_{s,\max-}F} \tag{30}$$

where $C_{ionloss}$ is calculated based on Eq. (13).

When a cell is charged to EOC, the $OCV_{\max}$ is described using two equilibrium potentials that are a function of stoichiometric numbers.

$$U_{eq+}(y_{EOC}) - U_{eq-}(x_{EOC}) = OCV_{\max} \tag{31}$$

The two variables, x_{EOC} and y_{EOC} are numerically solved using Eq. (31) and Eq. (29) and plotted in Fig. 6 with symbols of "X". The result shows that the x_{EOC} and y_{EOC} calculated above are less than x_{max} and y_{min}, respectively. Consequently, given the same $OCV_{\max}$, the anode electrode cannot be fully charged while cathode electrode can be over-discharged.

Similarly, when a cell is discharged to EOD, the $OCV_{\min}$ can be described as;

$$U_{eq+}(y_{EOD}) - U_{eq-}(x_{EOD}) = OCV_{\min} \tag{32}$$

where x_{EOD} and y_{EOD} are numerically solved and plotted in Fig. 6 with symbols of "X" and they become less than x_{min} and y_{max}, respectively. It shows that the cathode electrode cannot be fully charged while anode electrode can be over-discharged at the same $OCV_{\min}$ given. The analysis assumes that the amount of over-discharge is small enough not to cause any damage at cathode or anode active material.

By updating x_{EOC}, y_{EOC}, x_{EOD} and y_{EOD} in Eq. (26), the cell capacity considering loss of ions is calculated and plotted as blue curve in Fig. 8 (in the web version). The capacity fade increases with an increasing amount of loss of ions. However, the amount of ion loss is not the same as that of capacity loss, as is frequently assumed.

4.2. Effects of loss of ion and active material (AM) on capacity fade

When a certain amount of active anode material is lost, its

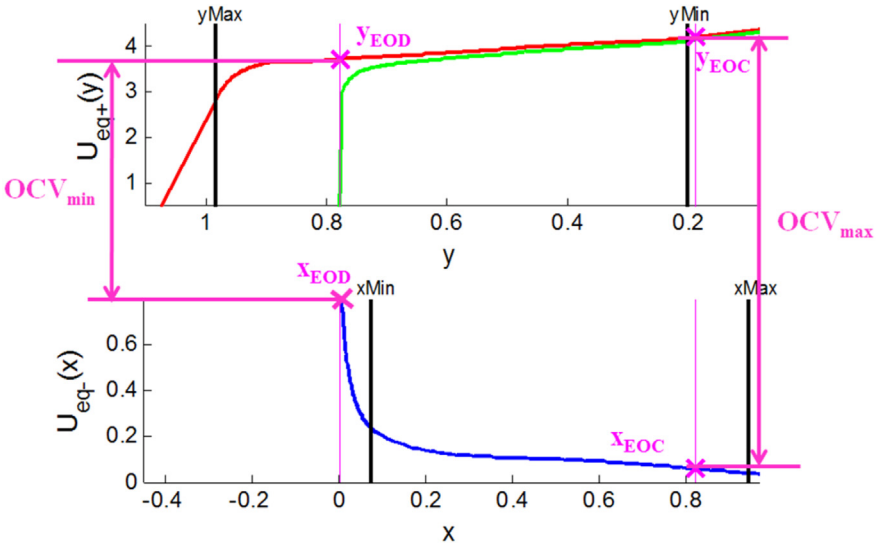

Fig. 7. Equilibrium potentials with EOD and EOC for an aged cell after loss of ion and active material.

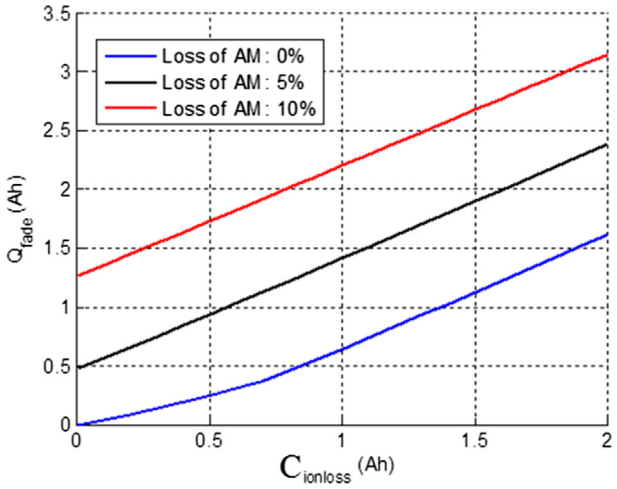

Fig. 8. Capacity fade as a function of loss of ion and active anode material.

Table 3
Test matrix considering different operating conditions.

	SOC cycling limits	Charging C-rates	Discharging C-rate	Temperature	Number of cycles
Baseline	25%–90%				
Effect of SOC	15%–80%	4C			
	5%–70%		4C	25 °C	600
Effect of charging C-rate	25%–90%	3C			
		2C			

volume fraction, ε_{s-}, decreases and the linear equation describing the relationship between y and x should be changed from Eq. (29) to

$$y = -\frac{(\varepsilon_{s0-} + \Delta\bar{\varepsilon}_{s-})\delta_- c_{s,\max,-}}{\varepsilon_{s+}\delta_+ c_{s,\max,+}}\left(x + x_{shift} - x_{\min}\right) + y_{\max} \qquad (33)$$

where $\Delta\bar{\varepsilon}_{s-}$ is the averaged value of the change of volume fraction obtained from Eq. (17), which is negative. After ε_{s-} is decreased, x changes faster with respect to y, based on Eq. (33). This mechanism can be represented by shrinking the x axis, as shown in Fig. 7.

In addition to ε_{s-}, loss of active material also affects x_{EOC}, y_{EOC}, x_{EOD} and y_{EOD} that can be recalculated using Eqs. (31)–(33) and are plotted in Fig. 7 with symbols of "X".

By updating x_{EOC}, y_{EOC}, x_{EOD}, y_{EOD} and ε_{s-} in Eq. (26), the cell capacity considering both loss of ions and loss of active materials is calculated and plotted in Fig. 8. The capacity fade increases with increasing amounts of both loss of ions and active materials.

5. Effects of operating conditions on degradation

To analyze the effects of operating conditions on degradation performance, the model for side reactions previously described has been integrated into the electrochemical-thermal model of a cell and simulations have been carried out using different operating conditions, as shown in Table 3. The number of cycles for baseline data was 600 at 25 °C. C-rates for both charging and discharging were 4C. The SOC cycling limit was 25%–90%. To study the degradation rate as a function of SOC, the SOC cycling limits were

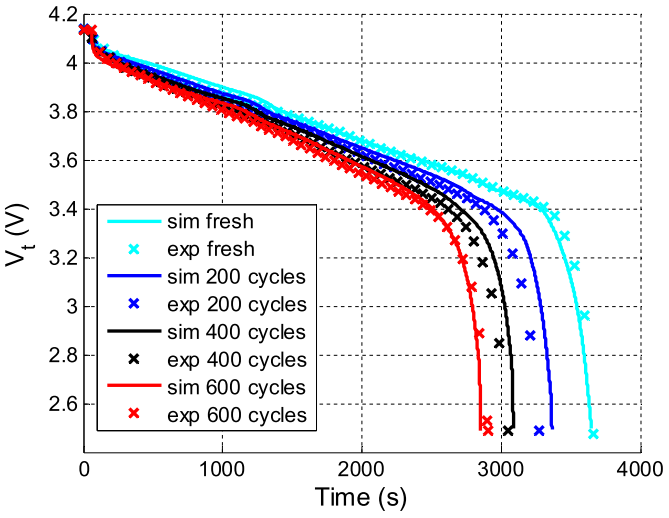

Fig. 9. 1C discharge curves of aged cell under baseline test conditions.

changed from 25%–90% to 15%–80% and 5%–70%. The range of each SOC cycling window was maintained at 65%. Also, the degradation rate as a function of the charging C-rate was considered. Three charging C-rates of 2C, 3C and 4C were used to study the effects on degradation rate. The discharging C-rate, ambient temperature and number of cycles were kept constant.

To validate the model, experiments were conducted under the same operating conditions shown in Table 3. For each case, a new cell was used. After every 20 cycles, a 1C current rate was applied to measure the cell capacity. Upon completion of the cycle, the cycled cells were set at 50% SOC and their impedances were measured using EIS. After each cycled cell was completely discharged and opened, samples of cells were cut off and analyzed using SEM to investigate the morphology and deposit layers. The description of the test equipment can be found in our previous work [9].

5.1. Degradation under the baseline condition

Discharging characteristics of the cell at 1C current rate and every 200 cycles are plotted in Fig. 9, where voltage drops and discharge times of the model are compared with those of experiments. Since the discharge processes start from 100% of SOC with a 1C (15.7 A) rate, it has taken an hour to completely discharge a fresh cell, whose capacity is 15.7 A h. However, when a cell is cycled, its capacity becomes less than 15.7 A h, so the discharge time becomes less than an hour because of capacity fade.

Therefore, as the number of cycles increases, the voltage under 1C discharge process decreases faster and the discharge time becomes shorter due to increased capacity fade. The voltage drop of the model tends to follow the experimental data at the beginning and middle of the discharge. At the end of the discharge, the simulated discharge time matches the experimental data for the fresh cell and cell at 600 cycles. However, there are some deviations at 200 and 400 cycles due to inaccurate estimations of capacity fade that might be caused by other degradation mechanisms that have not identified in this work, such as phase change of the cathode active material with the formation of an oxide layer, lithium plating, and decomposition of the separator [22,23].

For analysis of capacity fade, the calculated amount of ion loss, C_{ionloss}, capacity fade caused by ion loss, $Q_{fade,\text{ion}}$, and loss of active material, $Q_{fade,AM}$, are plotted in Fig. 10. The measured total capacity fade is plotted for validation as well. The total amount of capacity

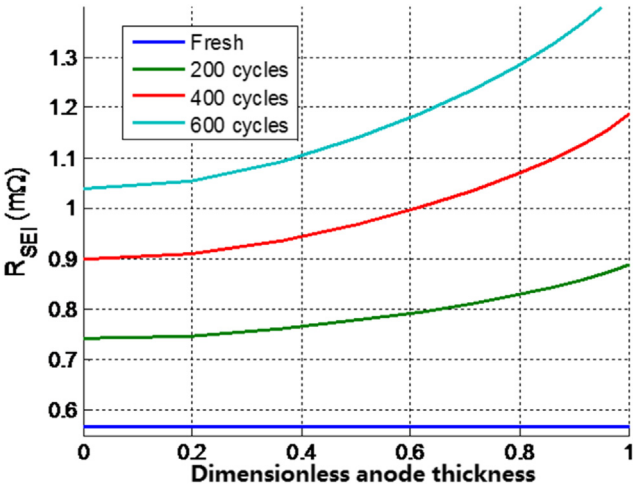

Fig. 11. Change in SEI resistance under baseline test conditions.

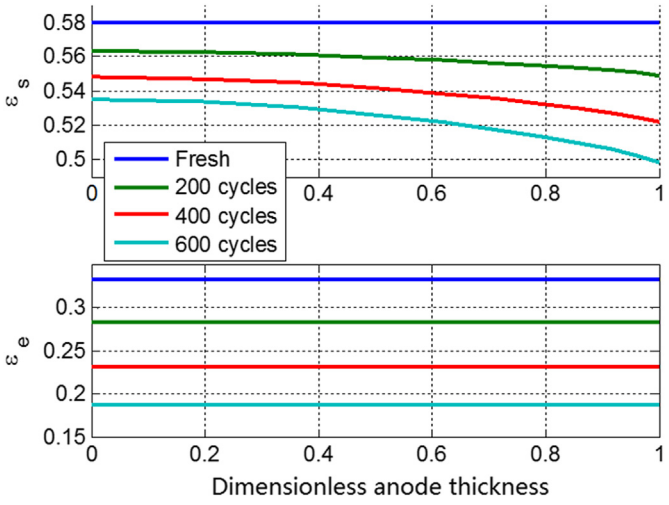

Fig. 12. Volume fractions of active material and electrolyte under baseline test conditions.

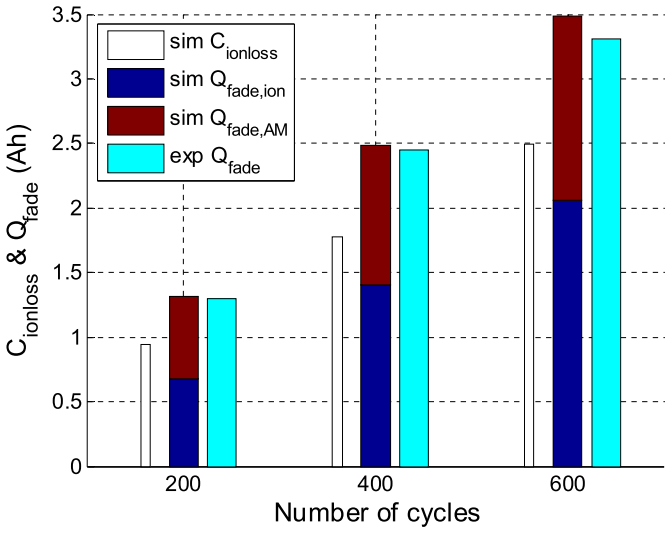

Fig. 10. Analysis of capacity fade under baseline test conditions.

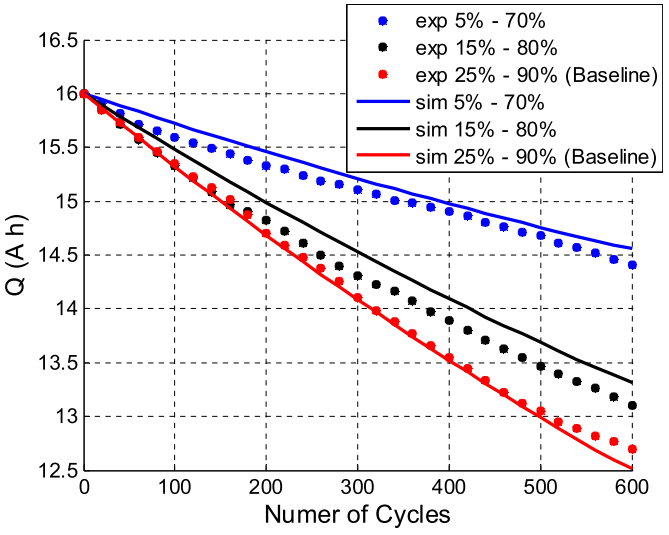

Fig. 13. Capacity fade at different SOC cycling limits.

fade from simulations and experiments at different cycles are comparable. Interestingly, the amount of ion loss, C_{ionloss}, is not the same as that of capacity fade caused by the ion loss, $Q_{fade,\text{ion}}$, as explained in section 4.1.

As the number of cycles increases, the capacity fade caused by loss of active material becomes slightly less than that by loss of ion. This finding might be interpreted by the phenomena that SEI isolates the anode particles that can be easily isolated at the beginning of cycling because of relative small particle size and poor contact with composite anode. Once these particles have been isolated, isolation of the rest large particles becomes difficult and consequently the increase of $Q_{fade,AM}$ becomes slow.

Based on the simulation results, the effects of cycling on SEI, volume fractions of active anode material and electrolyte are analyzed. SEI resistances as a function of anode thickness calculated using Eqs. (14)–(16) are plotted in Fig. 11. As the number of cycles increases, the SEI resistance tends to increase and the increase is large near the separator on the anode side because of the high ion concentrations that cause a high rate of side reaction.

The volume fraction of the active anode material, ε_s, and the electrolyte, ε_e, are calculated and plotted in Fig. 12. As the number of cycles increases, ε_s becomes less, particularly near the separator because of isolation of the active material by growing SEI layers, which can be seen in Eq. (17). Similarly, ε_e becomes less because of the side reactions that consume the electrolyte. It is assumed that there is no gradient of ε_e in the direction of anode thickness, based on Eq. (21).

5.2. Effects of SOC cycling limits on degradation

In real world operations, the SOC cycling limits vary depending upon operating modes. Effects of different SOC limits are investigated using the test conditions shown in the second and third row of Table 3. Calculated and measured capacity over the number of cycles under different SOC cycling limits are plotted in Fig. 13. Generally, capacity fade of the cell cycled at 25%–90% is the largest, followed by 15%–80% and 5%–70%. The model can predict the capacity fade well. The deviations might be caused by some other neglected degradation mechanism as indicated in literature, such as phase change of the cathode active material with the formation of an oxide layer, lithium plating, and decomposition of the separator [22,23].

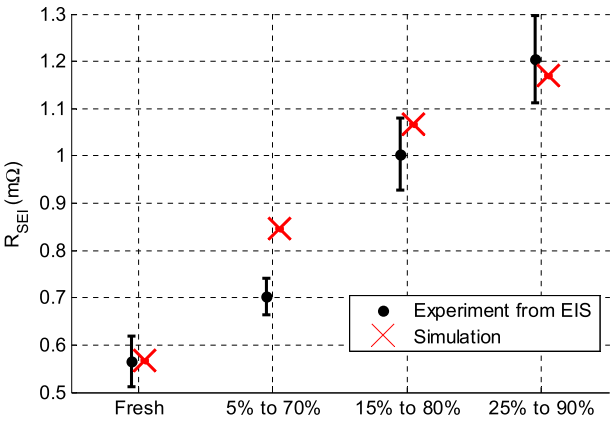

Fig. 15. SEI resistance of fresh cell and cells after 600 cycles.

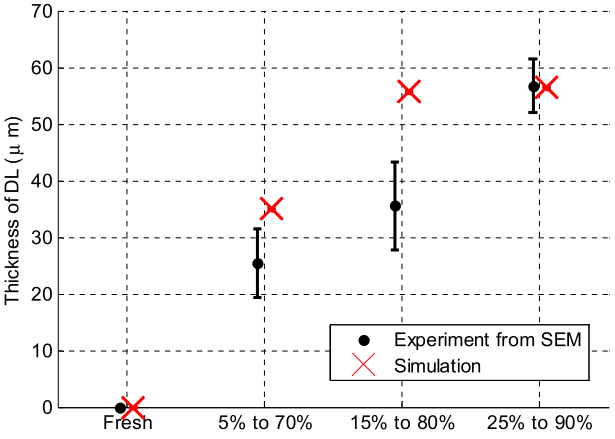

Fig. 16. Thickness of DL of fresh cell and cells after 600 cycles.

Calculated and measured discharging characteristics of the fresh and cycled cells after 600 cycles under different SOC cycling limits are plotted in Fig. 14, where the current rate was 1C. After cycled,

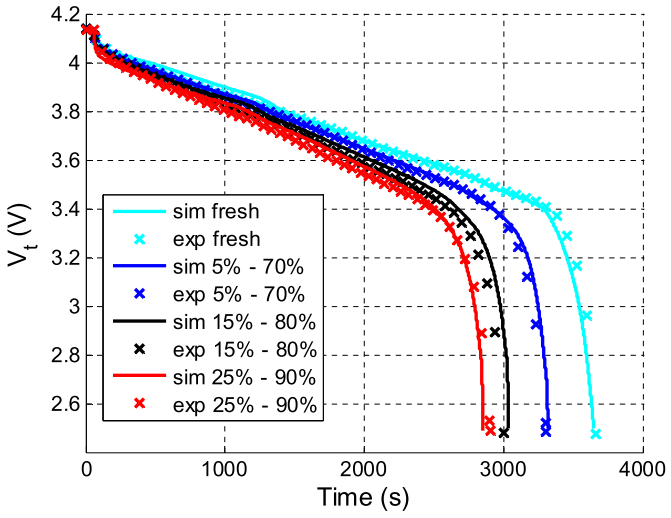

Fig. 14. 1C discharge curve at 600 cycles at different SOC cycling limits.

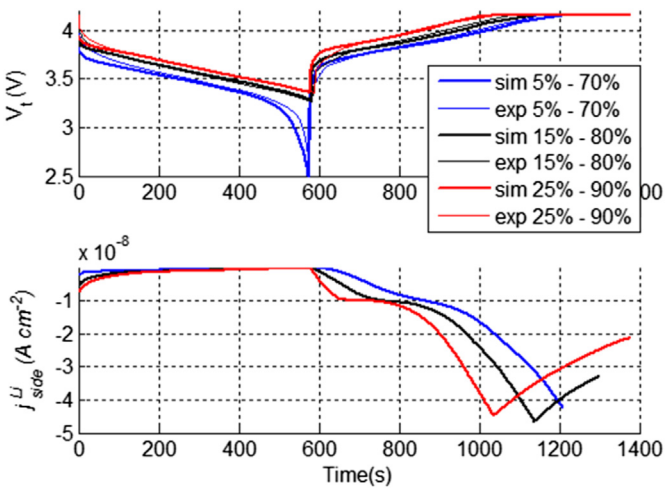

Fig. 17. Terminal voltage and side reaction rates in a discharge–charge cycle at different SOC cycling limits.

cells become quickly discharged because of the faded capacity. The higher the SOC limit is, the faster the cells are degraded.

The SOC limits also affect SEI resistance. The simulated and measured SEI resistances as a function of SOC limits are plotted in Fig. 15. The measured values of SEI are obtained from EIS analysis and this methodology is described in Appendix I. SEI resistance significantly increases as the SOC cycling limits move to the upper range. The model tends to follow the experimental data with some deviations.

Similarly, SOC cycling limits affect the formation of deposit layers. As a result, ion conductivity decreases and internal resistance increases. Calculated and measured thicknesses of the DL using Eq. (18) and SEM are plotted in Fig. 16. The thickness increases as SOC limits move to the upper range. The model tends to follow the data extracted from the SEM measurements. A few examples of SEM micrographs and measurements of DL are provided in Appendix II.

The results of capacity fade and resistance increase as shown above reveal that degradation is most severe in the cell operated at high SOC cycling limits, 25%–90%, followed by 15%–80% and 5%–70%. For more detailed analysis, the rate of side reactions j_{side}^{Li}, is analyzed since it determines the rates of all degradation processes caused by the side reactions.

The calculated and measured terminal voltages as well as calculated j_{side}^{Li} are plotted in Fig. 17 during a single discharge–charge cycle under different SOC cycling limits. When the cells are discharged, the terminal voltages decrease and the magnitude of j_{side}^{Li} decreases. When the cells are being charged with a constant current, the terminal voltages begin to increase and the magnitude of j_{side}^{Li} increases significantly. Finally, when the cell is charged with a constant voltage, the magnitude of j_{side}^{Li} decreases because of the decrease in charging current. The cell cycled under 25%–90% has the highest magnitude of j_{side}^{Li}, followed by 15%–80% and 5%–70%.

The variation of j_{side}^{Li} shown above is caused by the changes in $i_{0,side}$ and η_{side}, based on Eq. (10). On one hand, j_{side}^{Li} is proportional to $i_{0,side}$, which is a function of temperature, as summarized in Table 2. Since all operating conditions considered in this work have used the same ambient temperature, the temperature variations during operation were small so the effects of temperature on $i_{0,side}$ and j_{side}^{Li} were not significant and thus not analyzed in details. On the other hand, j_{side}^{Li} is very sensitively affected by the change of η_{side} because η_{side} is the variable in the exponential power term, as shown in Eq. (10). In addition, as seen from Eq. (11), η_{side} can be affected by other factors, so detailed analyses are performed. By substituting Eqs. (6), (7) and (12) with Eq. (11), a new expression for η_{side} is obtained;

$$\eta_{side} = \eta + U_{ce} + U_{eq-}^{\Theta}\left(x\right) - U_{eq,side}^{\Theta} \tag{34}$$

where

$$U_{ce} = \frac{RT}{2F}\ln\left(\frac{c_e}{c_{e0}}\right) \tag{35}$$

Hence, η_{side} includes four terms, where $U_{eq,side}^{\Theta}$ is considered a constant and the rest three terms, η, U_{ce} and $U_{eq-}^{\Theta}(x)$, are analyzed for one discharge–charge cycle, as shown in Fig. 18.

The first term is the activation overpotential of intercalation, η. The simulation results in Fig. 18 show that η is positive when the cell is being discharged and negative when the cell is being charged. This is true because η is proportional to the reaction rate of intercalation, j^{Li}, based on Eq. (5), so η should have the same sign with j^{Li}.

The second term is the potential change caused by ion concentration in electrolyte, U_{ce}, which originates from the Nernst equation, Eqs. (7) and (12). U_{ce} is positive when the cell is discharged and negative when the cell is charged. When the cell is discharged, ions are transported from anode to cathode through electrolyte according to the diffusion process shown in Table 1. Ion transport is driven by the gradient of ion concentration from high c_e region to low c_e region. Therefore, in the region of composite anode, c_e is larger than c_{e0} under discharging and smaller than c_{e0} under charging, which explains the signs of U_{ce} shown in Fig. 18.

The third term is the equilibrium potential of intercalation at anode, U_{eq-}^{Θ}. As expected, U_{eq-}^{Θ} decreases with the increase of SOC, as shown in Fig. 18.

In summary, η_{side} becomes more negative when SOC becomes high and when the cell is being charged rather than discharged. The magnitude of the side reaction rate increases if η_{side} becomes more

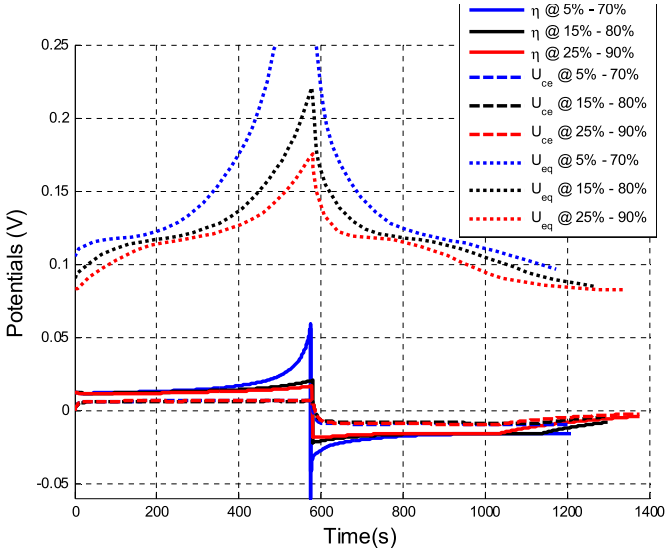

Fig. 18. Potentials that determine side reaction overpotential in a discharge–charge cycle under different SOC cycling limits.

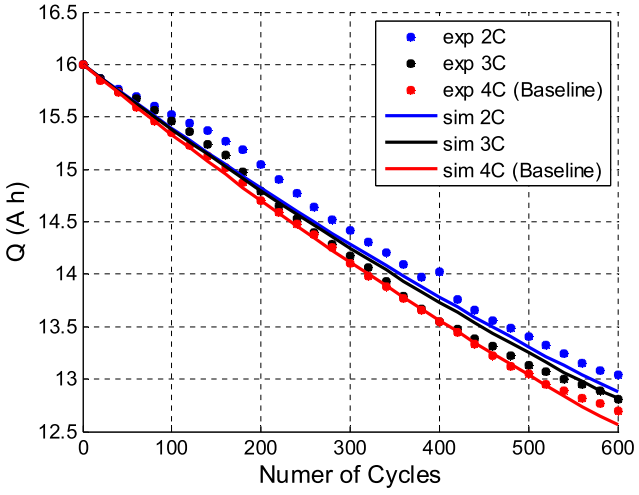

Fig. 19. Effect of charging C-rates on capacity fade.

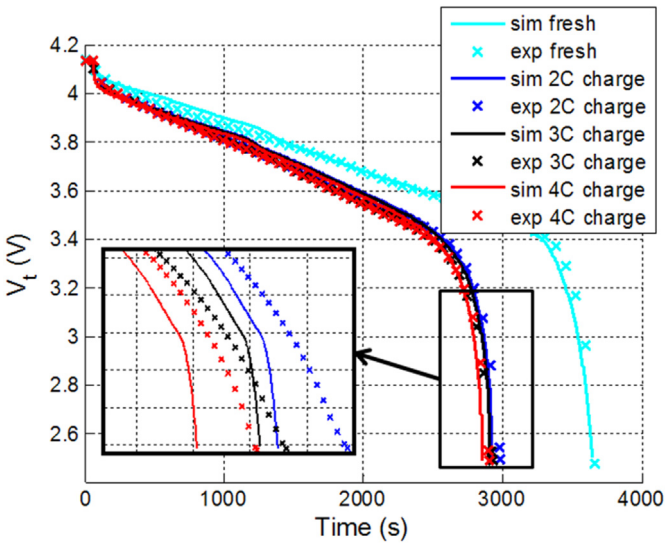

Fig. 20. 1C discharge curve at 600 cycles at different charging C-rates.

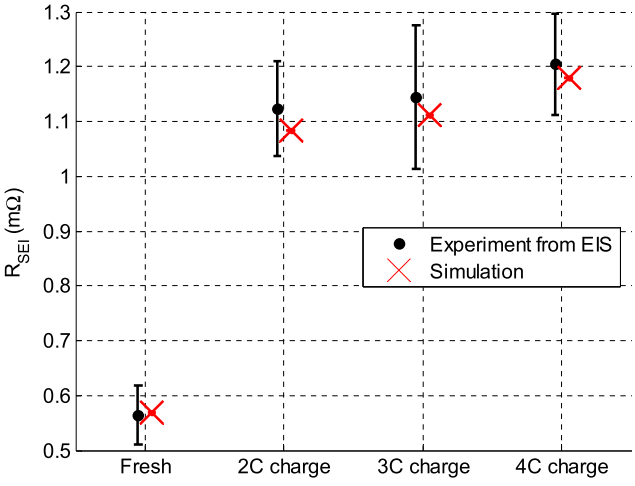

Fig. 21. SEI resistance of fresh cell and cells after 600 cycles.

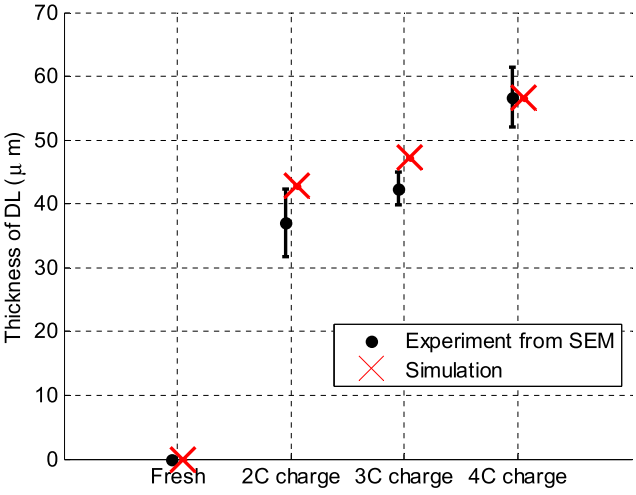

Fig. 22. Thickness of DL of fresh cell and cells after 600 cycles.

negative, as shown in Eq. (10). Consequently, charging a cell to higher SOC leads to a larger rate of side reactions, which eventually accelerates degradation.

5.3. Effects of charging C-rate on degradation

In real world operations, the C-rates at charging vary depending upon vehicle operating conditions. Effects of charging C-rates on capacity fade are investigated using the test conditions shown in the fourth and fifth row of Table 3. Calculated and measured capacity over the number of cycles under three charging C-rates are plotted in Fig. 19. The capacity fade of the cell cycled at 4C charging rate is the largest, followed by 3C and 2C. However, the capacity fade under different charging rates is not clearly distinctive. The model can predict the capacity fade well with some deviations, which might be caused by some other neglected degradation mechanisms as indicated in the literature review.

Calculated and measured discharging characteristics of the fresh and cycled cells after 600 cycles as a function of charging C-rates are plotted in Fig. 20, where the current rate was 1C. After being cycled, the cells become discharged quickly because of the faded capacity. When the charging C-rate becomes larger, the capacity fade is slightly increased.

The charging C-rates also affect SEI resistance. The simulated and measured SEI resistances as a function of charging C-rates are plotted in Fig. 21. SEI resistance slightly increases as the charging C-rate increases. The simulation result tends to follow the experimental data with some deviations.

Similarly, the formation of the DL is affected by charging C-rates. Calculated and measured thicknesses of the DL using Eq. (18) and SEM are plotted in Fig. 22. The thickness increases with the increase of charging C-rates. The simulation results tend to follow the data extracted from the SEM measurements.

The results of capacity fade and resistance increase as shown above reveal that the degradation is worsening when the charging C-rate is high. Similar to the previous section, analyses of j_{side}^{Li} and η_{side} are conducted again with three different charging C-rates.

The calculated and measured terminal voltages as well as calculated j_{side}^{Li} are plotted in Fig. 23 for a single discharge–charge cycle under different charging C-rates. When charged with high C-

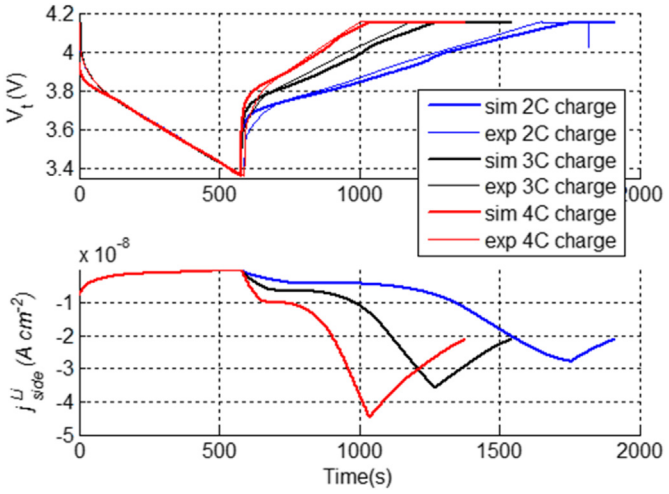

Fig. 23. Terminal voltage and side reaction rates in a discharge–charge cycle at different charging C-rates.

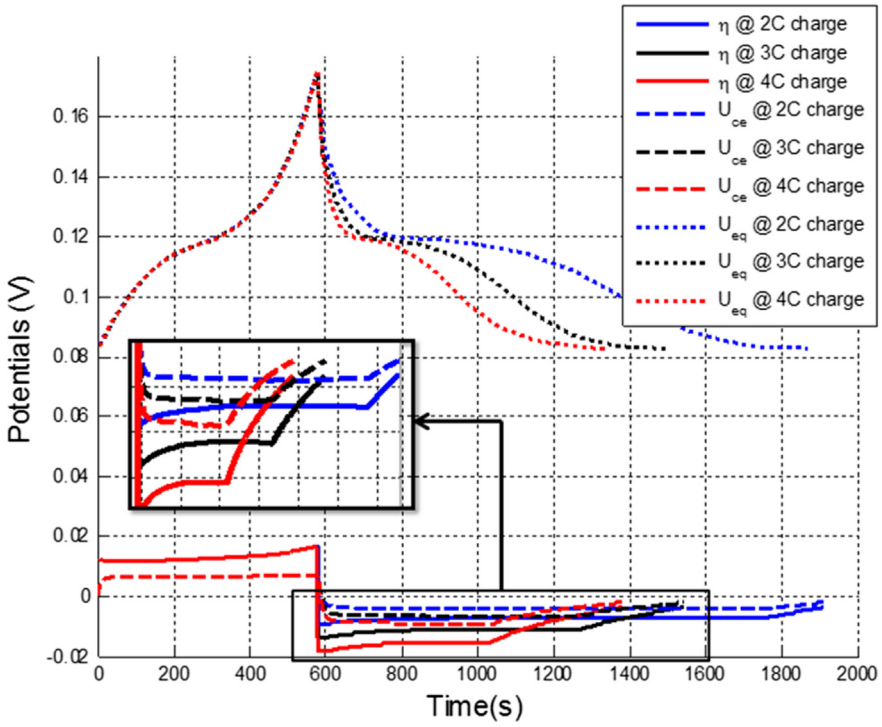

Fig. 24. Potentials that determine side reaction overpotential in a discharge–charge cycle at different charging C-rates.

rates, the magnitude of j_{side}^{Li} becomes large as does the instantaneous degradation rate.

As explained previously, j_{side}^{Li} is predominantly affected by η_{side} that is a function of the three variables, η, U_{ce} and U_{eq}^{Θ}. The three variables are calculated and plotted in Fig. 24.

As the charging C-rate increases, η has a negative value and becomes smaller. As explained in the previous section using Eq. (5), η is a function of j^{Li}, so the magnitude of η increases as the charging C-rate increases.

Similarly, U_{ce} also becomes small as charging C-rate increases. The increased charging C-rate leads to a higher gradient of ion concentration in the electrolyte. Consequently, c_e in composite anode becomes low and U_{ce} gets decreased with the increase of charging C-rate.

In addition, U_{eq}^{Θ} decreases rapidly when the cell is charged with increased C-rate because of the resulting high SOC.

The analysis of effects of C-rates on performance show that η_{side} decreases and j_{side}^{Li} becomes significantly high when the charging C-rate is increased. However, dependence of the degradation upon the C-rates was not clearly distinctive at the same number of cycles (Figs. 19–22) because the degradation is determined by integration of j_{side}^{Li} over time, according to Eqs. (13), (14) and (18). When C-rates are high, charging process takes shorter time although the magnitude of j_{side}^{Li} is large. Consequently, contribution of charging C-rates to degradation is limited, as predicted by the model, which agrees with the trend of experimental data (Figs. 19–22).

6. Conclusion

A variety of experimental analysis has shown that the side reactions are the main cause for degradation process in lithium ion batteries. The side reactions are mathematically described using the Tafel equation and the corresponding degradation processes are modeled based on physical principles. The model is incorporated into the electrochemical-thermal model developed previously, where the main reaction is modeled based on linear kinetics simplified from the Butler–Volmer equation. The integrated model is then validated against experimental data obtained from large format LiPB NMC/Carbon cells. Numerical and experimental analysis have shed light on the mechanisms of capacity and power fade as well as their dependencies on different operating conditions.

The key findings are as follows;

- Not only the loss of ion, but also the loss of active anode material are the factors that cause capacity fade. The mechanisms are illustrated by analysis of the two factors on EOC and EOD determined by two equilibrium potentials and OCVs.
- The side reactions produce deposit layers and increase the thickness of SEI layer, which leads to power fade. Simulated growths of both layers are confirmed quantitatively characterized using SEM and EIS.
- The charging process causes more degradation than the discharging process. The overpotential of the side reactions (η_{side}) is small during charging and large during discharge. Consequently, the rate of side reactions during charging is larger than that during discharging.
- Cycling at high SOC accelerates the degradation processes because the equilibrium potential of anode becomes low, which leads to low η_{side} and large rate of side reactions.
- Charging at high C-rate significantly and instantaneously increases the degradation rate. However, the dependence of degradation upon the C-rates was not clearly distinctive at the same number of cycles, because high C-rate leads to not only increase of side reaction rate but also reduction of charging time.

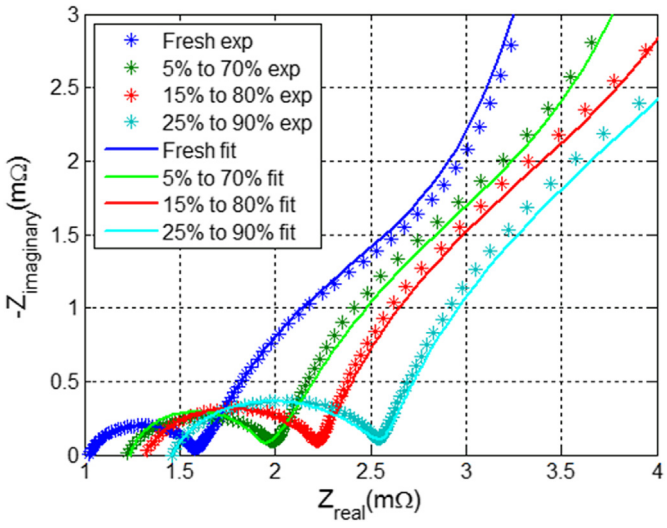

Fig. 25. EIS Impedance of cells cycled under different SOC cycling limits.

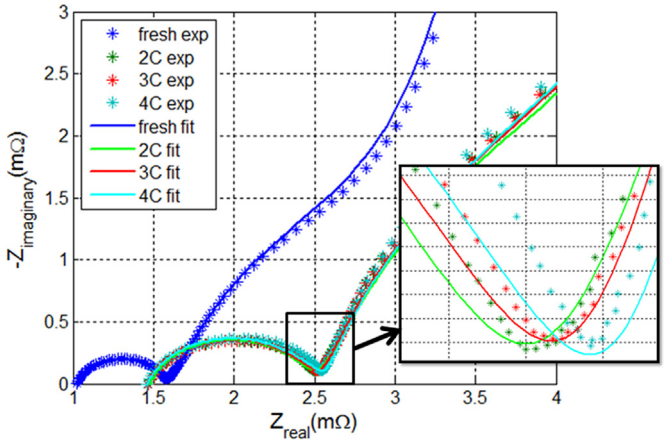

Fig. 26. EIS Impedance of cells cycled under different charging rates.

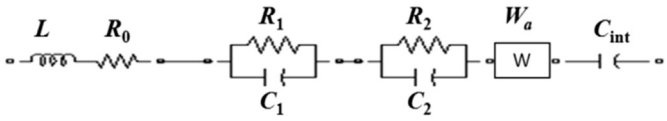

Fig. 27. EIS equivalent circuit model.

Future work will include

- Extend the model that considers other chemical processes for the degradation dependent upon different temperatures and driving profiles.
- Conduct extra self-discharge tests to study effects of the reversible and irreversible self-discharge rates, so that $i_{0,side}$ can be better estimated.

Appendix I. Estimation of SEI resistance using impedance measured by EIS

The impedances measured by EIS equipment are plotted as markers in Fig. 25 and Fig. 26. The impedance of a fresh cell consists of a complete semicircle and a linearly increasing slope weakly superposed with another semicircle. The impedance plots of cycled cells tend to be shifted to the right side with increased radius of the first semicircle. An equivalent circuit model, as shown in Fig. 27, is used to approximate the impedance behavior of a cell given by the EIS data, where R_1 represents the SEI resistance that predominantly determines the shape of the first semi-circle [24–27]. The SEI resistances obtained from the equivalent circuit model are then compared with R_{SEI} calculated by the degradation model, which is shown in Figs. 15 and 21.

Appendix II. Measurement of deposit layers using SEM

The cycled cells were completely discharged and then dismantled for postmortem analysis. Multiple small samples were harvested from different locations of each cell, which is prepared in the globe box with a high purity argon atmosphere. Separators were removed from anode and cathode samples when conducting the analysis. Two images for anodes from a fresh and a degraded cell taken by SEM are shown in Fig. 28, where the anode particles of the cycled cells are covered by white deposits. These deposits are randomly and non-uniformly dispersed all over the carbon particles and the ratio of the coverage has not changed significantly from a cell to others. In addition, images of cross-sections of a fresh anode and a degraded anode taken by SEM are shown in the left and right of Fig. 29, respectively, where a thick deposit layer is formed at the anode of degraded cell. The thickness of deposit layer measured from multiple samples at different locations of a cell using SEM are listed in Table 4. The average thickness of deposit layers is used to compare with the prediction from the degradation model, as shown in Figs. 16 and 22.

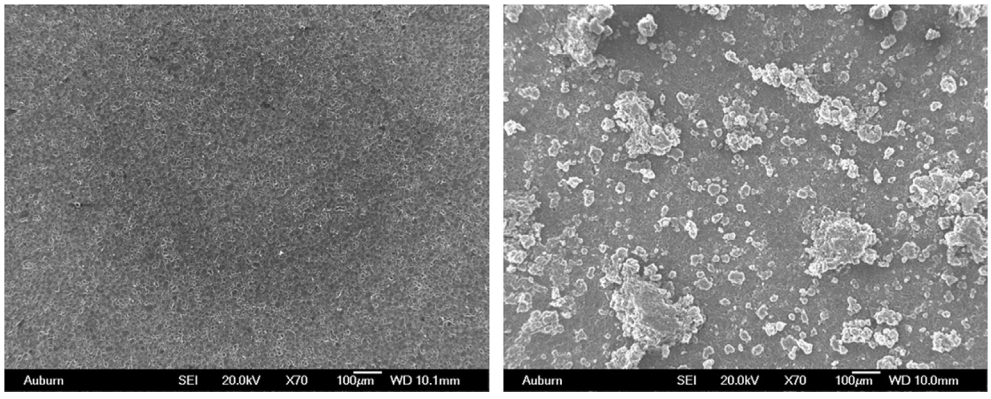

Fig. 28. SEM of a fresh anode (left) and a degraded anode (right) after 600 cycles under 15%–80% SOC using 4C charge rate.

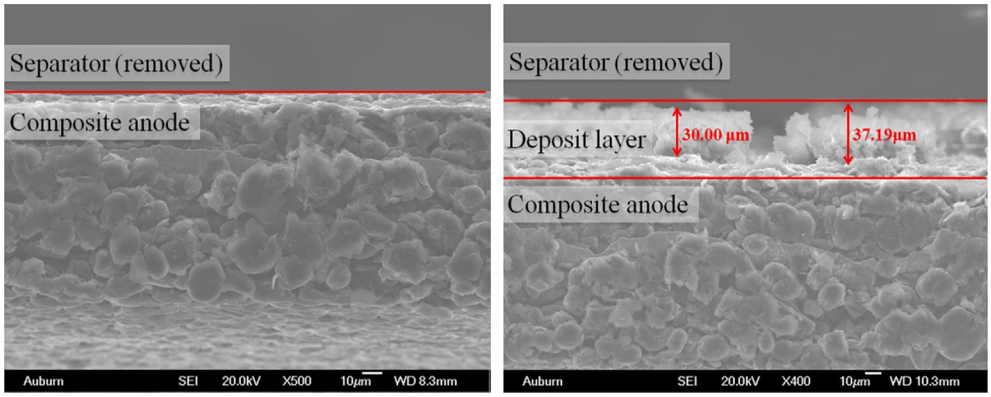

Fig. 29. SEM of cross-sections of a fresh anode (left) and a degraded anode (right) after 600 cycles under 15%–80% SOC using 4C charge rate.

Table 4
Thickness of deposit layers.

Test conditions	Thickest deposit	Thinnest deposit	Averaged thickness (among 15 measurements)	Standard deviation (among 15 measurements)
25%–90%; 4C charging	61.45 μm	50.02 μm	56.73 μm	4.71 μm
15%–80%; 4C charging	47.83 μm	22.27 μm	35.55 μm	7.83 μm
5%–70%; 4C charging	39.94 μm	16.13 μm	25.47 μm	6.09 μm
25%–90%; 3C charging	45.30 μm	40.12 μm	42.42 μm	2.64 μm
25%–90%; 2C charging	42.95 μm	32.79 μm	37.07 μm	5.27 μm

Appendix III. Model parameters

The model parameters for a fresh cell are shown in Table 5. The parameters for modeling side reactions and degradations are shown in Table 6.

Table 5
Model parameters for a fresh cell.

Category	Parameter	Negative electrode	Separator	Positive electrode	Unit
Geometry and volume fractions	Thickness, δ	50×10^{-4}	25.4×10^{-4}	36.4×10^{-4}	cm
	Particle radius, r_s	1×10^{-4}		1×10^{-4}	cm
	Active material volume fraction, ε_s	0.58		0.5	
	Polymer phase volume fraction, ε_p	0.048	0.5	0.11	
	Conductive filler volume fraction, ε_f	0.04		0.06	
	Porosity, ε_e	0.332	0.5	0.33	
Li^+ concentrations	Stoichiometry at 0% *SOC*: $x_{0\%}$, $y_{0\%}$	0.126		0.936	
	Stoichiometry at 100% *SOC*: $x_{100\%}$, $y_{100\%}$	0.676		0.442	
	Average electrolyte concentration, c_e	1.2×10^{-3}	1.2×10^{-3}	1.2×10^{-3}	mol cm^{-3}
	Exchange current density coefficient, k_{i0}	12.9		6.28	A cm^{-2}
Kinetic and transport properties	Charge–transfer coefficient, α_a, α_c	0.5, 0.5		0.5, 0.5	
	Solid phase diffusion coefficient, D	2.0×10^{-12}		3.7×10^{-12}	$cm^2\ s^{-1}$
	Solid phase conductivity, σ	1		0.1	S cm^{-1}
	Electrolyte phase Li^+ diffusion coefficient, D_e	2.6×10^{-6}	2.6×10^{-6}	2.6×10^{-6}	$cm^2\ s^{-1}$
	Bruggeman's porosity exponent, p	1.5	1.5	1.5	
	Electrolyte phase ionic conductivity, κ	$15.8c_e \exp(-13472c_e^{1.4})$		$15.8c_e \exp(-13472c_e^{1.4})$	S cm^{-1}
	Li^+ transference number, t_+^0	0.363	0.363	0.363	

Table 6
Model parameters of side reactions and degradations.

Parameter	Value	Source
Exchange current of side reactions, $i_{0,s}$ (A cm^{-2})	0.39×10^{-11} at 0 °C 2.28×10^{-11} at 25 °C 6.50×10^{-11} at 50 °C	Optimized by comparing simulation to the self-discharge data
Equilibrium potential of side reactions, $U_{eq,s}$ (V)	0.21	Optimized by comparing simulation to the self-discharge data
Cathodic symmetric factor of side reactions, $\alpha_{c,side}$	0.70	Optimized by comparing simulation to the degradation data under different SOC cycling limits. The value falls in an acceptable range provided by Ref. [28]
Molar volume of SEI, $\bar{V}_{SEI}$ (cm^3/mol)	2	Obtained by assuming the initial thickness of SEI is 2 nm
ionic conductivity of SEI, κ_{SEI} (S cm^{-1})	2.3×10^{-8}	Optimized by comparing simulation to the SEI resistance obtained from EIS
isolation rate of active anode materials due to SEI, k_{iso}	27.3	Optimized by comparing simulation to measured capacity fade
molar volume of DL, $\bar{V}_{DL}$ (cm^3/mol)	7560	Optimized by comparing simulation to the thickness of DL measured by SEM
ionic conductivity of DL, κ_{DL} (S cm^{-1})	1.26×10^{-2}	Optimized by comparing simulation to the terminal voltage under cycling
molar volume of electrolyte, $\bar{V}_e$ (cm^3/mol)	325	Optimized by comparing simulation to the terminal voltage under cycling

References

[1] P. Ramadass, B. Haran, P. Gomadam, R. White, B. Popov, J. Electrochem. Soc. 151 (2004) A196–A203.
[2] P. Arora, R. White, M. Doyle, J. Electrochem. Soc. 145 (1998) 3647–3667.
[3] S. Santhanagopalan, Q. Zhang, K. Kumaresan, R. White, J. Electrochem. Soc. 155 (2008) A345–A353.
[4] G. Sikha, B. Popov, R. White, J. Electrochem. Soc. 151 (2004) A1104–A1114.
[5] H. Ploehn, P. Ramadass, R. White, J. Electrochem. Soc. 151 (2004) A456–A462.
[6] Q. Zhang, R. White, J. Power Sources 179 (2008) 793–798.
[7] D. Aurbach, M. Levi, E. Levi, A. Schechter, J. Phys. Chem. B 101 (1997) 2195–2206.
[8] P. Verma, P. Maire, P. Novak, Electrochim. Acta 55 (2010) 6332–6341.
[9] R. Fu, S.Y. Choe, V. Agubra, J. Fergus, J. Power Sources 261 (2014) 120–135.
[10] S. Shi, P. Lu, Z. Liu, Y. Qi, L. Hector, H. Li, S. Harris, J. Am. Chem. Soc. 134 (2012) 15476–15487.
[11] J. Vetter, P. Novak, M. Wagner, C. Veit, K. Moller, J. Besenhard, M. Winter, M. Wohlfahrt-Mehrens, C. Vogler, A. Hammouche, J. Power Sources 147 (2005) 269–281.
[12] P. Ramadass, B. Haran, R. White, B. Popov, J. Power Sources 123 (2003) 230–240.
[13] M. Safari, M. Morcrette, A. Teyssot, C. Delacourt, J. Electrochem. Soc. 156 (2009) A145–A153.
[14] G. Ning, R. White, B. Popov, Electrochim. Acta 51 (2006) 2012–2022.
[15] D. Aurbach, J. Power Sources 89 (2000) 206–218.
[16] M. Broussely, S. Herreyre, P. Biensan, P. Kasaztejna, K. Nechev, R. Staniewicz, J. Power Sources 97–98 (2001) 13–21.
[17] S. Sloop, J. Kerr, K. Kinoshita, 119–121 (2003) 330–337.
[18] R. Yazami, Y. Reynier, Electrochim. Acta 47 (2002) 1217–1223.
[19] G. Sikha, P. Ramadass, B. Haran, R. White, B. Popov, J. Power Sources 122 (2003) 67–76.
[20] R. Fu, M. Xiao, S.Y. Choe, J. Power Sources 224 (2013) 211–224.
[21] M. Xiao, S. Choe, J. Power Sources 218 (2012) 357–367.
[22] S. Choi, H. Lim, J. Power Sources 111 (2002) 130–136.
[23] Y. Gao, J. Dahn, Solid State Ionics 84 (1996) 33–40.
[24] R. Bouchet, S. Lascaud, M. Rosso, J. Electrochem. Soc. 150 (2003) A1385–A1389.
[25] P. Moss, G. Au, E. Plichta, J. Zheng, J. Electrochem. Soc. 157 (2010) A1–A7.
[26] G. Ning, B. Haran, B. Popov, J. Power Sources 117 (2003) 160–169.
[27] B. Ratnakumar, M. Smart, S. Surampudi, in: Battery Conference on Applications and Advances, The Seventeenth Annual, 2002.
[28] J. Newman, K. Thomas-Alyea, Electrochemical Systems, third ed., 2004.